

# Efficient transport of indirect excitons in a van der Waals heterostructure

Zhiwen Zhou,<sup>1</sup> W. J. Brunner,<sup>1</sup> E. A. Szwed,<sup>1</sup> H. Henstridge,<sup>1</sup> L. H. Fowler-Gerace,<sup>1</sup> and L. V. Butov<sup>1</sup>

<sup>1</sup>*Department of Physics, University of California San Diego, La Jolla, CA 92093, USA*

(Dated: July 8, 2025)

Exciton transport is fundamental for understanding transport phenomena in bosonic systems and for embracing excitation energy transfer in materials. Spatially indirect excitons (IXs) are composed of electrons and holes in separated layers. Long IX lifetimes allow them to form quantum bosonic states and travel long distances. In this work, we measured IX transport in a MoSe<sub>2</sub>/WSe<sub>2</sub> van der Waals heterostructure by time-resolved photoluminescence imaging. These measurements probe the kinetics of IX cloud expansion and reveal the transport characteristics. We found IX transport with anomalously high diffusivity, orders of magnitude higher than for regular diffusive exciton transport in van der Waals heterostructures. This efficient IX transport agrees with long-range ballistic transport and is consistent with the Bose-Hubbard theory prediction of superfluid in moiré superlattices.

Excitons, the bound pairs of electrons and holes, are composite bosons [1]. Spatially indirect excitons (IXs), also known as interlayer excitons, are formed by electrons and holes in separated layers in a heterostructure (HS) [2]. Due to the layer separation, the IX lifetimes are orders of magnitude longer than lifetimes of spatially direct excitons (DXs) [3]. The long lifetimes allow IXs to cool below the temperature of quantum degeneracy and form quantum bosonic states [4]. Furthermore, the long IX lifetimes give an opportunity to achieve long-range exciton transport [5]. Due to these properties, IXs can be used for studying transport phenomena in quantum bosonic states and for exploring efficient excitonic energy transfer in materials.

IX transport phenomena are intensively studied in various materials platforms, including GaAs HS [5–21], GaN HS [22], and ZnO HS [23]. Recently, IX transport studies were started in van der Waals (vdW) HS composed of atomically thin layers of transition metal dichalcogenides (TMD). VdW TMD HS offer a unique platform for exploring exciton transport. First, excitons in vdW TMD HS, both DXs [24–26] and IXs [27, 28], have high binding energies reaching hundreds of meV. In comparison, IX binding energies in HS formed from III-V or II-VI semiconductors are significantly lower: e.g. 3 – 4 meV in GaAs/AlGaAs HS [29, 30] and 30 meV in ZnO HS [31]. The high binding energies make IXs in vdW TMD HS stable at room temperature. Furthermore, the superfluidity temperature that can be achieved with excitons is proportional to the exciton binding energy and the high IX binding energies in vdW TMD HS give an opportunity to realize high-temperature superfluidity [27]. Second, IXs in periodic potentials of moiré superlattices in vdW TMD HS give an opportunity to explore the Bose-Hubbard (BH) physics [32–36].

Exciton transport phenomena are intensively studied both with DXs in TMD monolayers [37–43] and with IXs in vdW TMD HS [44–63]. These studies showed that disordered in-plane potentials, including disordered moiré potentials, suppress diffusive IX transport due to IX localization and scattering. In particular, even in the case

of long IX lifetimes, diffusive IX transport in vdW TMD HS is characterized by low  $1/e$  decay distances  $d_{1/e}$ , up to a few micrometers [44–59]. IX transport with high  $d_{1/e}$ , substantially exceeding  $d_{1/e}$  for diffusive IX transport and reaching 100 micrometers, was recently reported [64, 65]. However, these reports lacked the direct measurements of IX transport that could establish the nature of this phenomenon.

In this work, we studied IX transport in a MoSe<sub>2</sub>/WSe<sub>2</sub> vdW HS by time-resolved imaging that directly measures the kinetics of IX photoluminescence (PL) cloud expansion and reveals the IX transport characteristics. We found IX transport with the anomalously high diffusivity, orders of magnitude higher than for regular diffusive IX transport in vdW TMD heterostructures. This efficient IX transport agrees with long-range ballistic transport.

## Experimental results

We study MoSe<sub>2</sub>/WSe<sub>2</sub> HS where adjacent MoSe<sub>2</sub> monolayer and WSe<sub>2</sub> monolayer form the separated electron and hole layers for IXs [66]. The HS details are presented in Supplementary Information (SI).

IXs are optically generated by focused laser excitation with the laser excitation energy resonant to DX in WSe<sub>2</sub> HS layer. The laser pulses have step-like rectangular shape with 80 ns pulse width, 0.3 ns edge sharpness, and 300 ns pulse period. The IX transport is measured by time- and spatially-resolved optical imaging. The measurement details are presented in SI.

After the onset of laser pulse, the IX cloud expands due to IX transport from the excitation spot. Figure 1a shows the kinetics of the IX signal profiles  $I(x, t)$ . The spatial extension of IX cloud is characterized by its  $1/e$  decay distance  $d_{1/e}(t)$  that is determined by least-squares exponential fit to  $I(x, t)$  in the HS (Fig. 1a).

Figures 1b-d show the kinetics of  $d_{1/e}(t)$  for different temperatures  $T$  and laser excitation powers  $P_{\text{ex}}$ . The enhancement of  $d_{1/e}(t)$  with time quantifies the kinetics of the IX cloud expansion due to IX transport. The efficient IX transport is observed in a certain range of tempera-

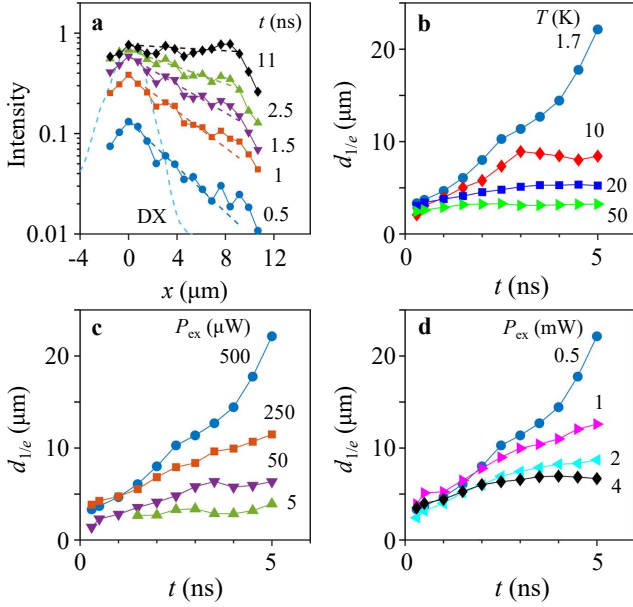


FIG. 1: Kinetics of IX cloud expansion. (a) IX PL spatial profiles  $I(x)$  vs. time  $t$  after the start of laser excitation pulse. IXs are created by the laser excitation. The excitation spot is centered at  $x = 0$  and is shown by cyan dotted line that presents the DX PL profile in WSe<sub>2</sub> monolayer and is close to the laser profile for short-range DX transport. The dashed lines show least-squares exponential fits to the decays of the IX cloud profiles  $I(x, t)$  to exponential decays in the region from the excitation spot to the HS edge,  $x = 0 - 9 \mu\text{m}$ . (b-d) The  $1/e$  decay distance of the IX cloud profiles  $d_{1/e}$  vs.  $t$  for different temperatures  $T$  (b) and laser excitation powers  $P_{\text{ex}}$  (c,d).  $P_{\text{ex}} = 0.5 \text{ mW}$  in (a,b),  $T = 1.7 \text{ K}$  in (a,c,d). The IX cloud expands and  $d_{1/e}$  increases with time due to IX transport. The efficient IX transport is observed in a certain range of temperatures and densities, e.g. at  $T = 1.7 \text{ K}$  and  $P_{\text{ex}} = 0.5 \text{ mW}$  [blue dots in (b-d)]. Less efficient IX transport is observed at high temperatures (b) and at lower (c) or higher (d) excitation densities.

tures and densities, e.g. for  $T = 1.7 \text{ K}$  and  $P_{\text{ex}} = 0.5 \text{ mW}$  (Fig. 1a-d). Less efficient IX transport is observed at high temperatures (Fig. 1b) and at lower (Fig. 1c) or higher (Fig. 1d) excitation densities.

### Analysis of experimental data

We compared the IX transport measurements with simulations. First, we compared the measured IX transport with diffusive transport described by the diffusion equation for IX density  $n$

$$\frac{\partial n}{\partial t} = D\Delta n + \Lambda - \frac{n}{\tau} \quad (1)$$

where the first term describes IX diffusion, the second IX generation by laser excitation, and the third IX recombination. The IX generation profile  $\Lambda(x)$  is given by the DX PL profile in WSe<sub>2</sub> monolayer that is close to the laser profile for the short-range DX transport (Fig. 1a). The IX

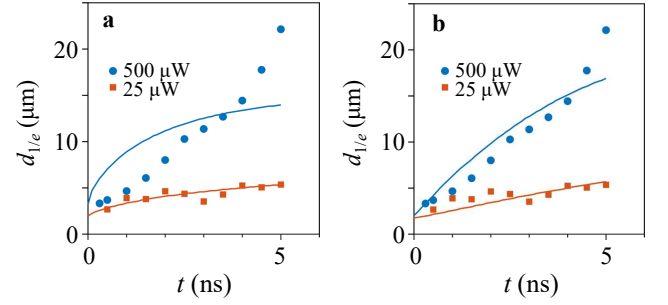


FIG. 2: Simulations of IX cloud expansion. The measured IX cloud expansion  $d_{1/e}(t)$  is shown by blue points for the excitation power  $P_{\text{ex}} = 500 \mu\text{W}$  and by red squares for  $P_{\text{ex}} = 25 \mu\text{W}$ . The simulated  $d_{1/e}(t)$  for diffusive (a) and ballistic (b) IX transport are shown by lines. In the simulations, the IX diffusivity  $D$  for diffusive transport (a) and IX velocity  $v$  for ballistic transport (b) are estimated by least-squares fit of the kinetics of exciton cloud expansion  $d_{1/e}(t)$  simulated with Eq. 1 and Eq. 2, respectively, to the measured  $d_{1/e}(t)$ . The obtained estimates for  $D$  and  $v$  are presented in Fig. 3 and Fig. 4. The laser excitation pulse starts at  $t = 0$ .  $T = 1.7 \text{ K}$ .

generation by laser excitation pulse with the rectangular step-like shape starts at  $t = 0$ . The IX recombination lifetime  $\tau$  is estimated from the measurements of the decay kinetics of the spatially integrated IX signal after the excitation pulse end. The measurements of  $\tau$  are outlined in SI. The IX diffusivity  $D$  is estimated by least-squares fit of the kinetics of exciton cloud expansion  $d_{1/e}(t)$  simulated with Eq. 1 to the measured  $d_{1/e}(t)$  (Fig. 2a).

We also compared the measured IX transport with ballistic transport described by the equation

$$\frac{\partial n}{\partial t} = -v\nabla n + \Lambda - \frac{n}{\tau} \quad (2)$$

where the first term describes IX transport with velocity  $v$ . The second and the third terms describe the IX generation and recombination and are similar to the corresponding terms in Eq. 1. The IX velocity  $v$  is estimated by least-squares fit of the kinetics of exciton cloud expansion  $d_{1/e}(t)$  simulated with Eq. 2 to the measured  $d_{1/e}(t)$  (Fig. 2b).

For the HS geometry elongated along the  $x$  direction, as outlined in SI, the IX transport is measured along  $x$  and is approximated in the simulations as one dimensional. The obtained estimates for the IX diffusivity  $D$  and velocity  $v$  are presented in Fig. 3 and Fig. 4.

### Discussion

*Anomalously high diffusivity and mean free path of IXs.* For the estimates using the diffusion equation (Eq. 1), the IX diffusivity reaches  $D \sim 10^3 \text{ cm}^2/\text{s}$  (Fig. 3). This value is significantly higher than the similarly determined IX diffusivities in time-resolved optical measurements of diffusive IX transport in vdW TMD HS, which reach

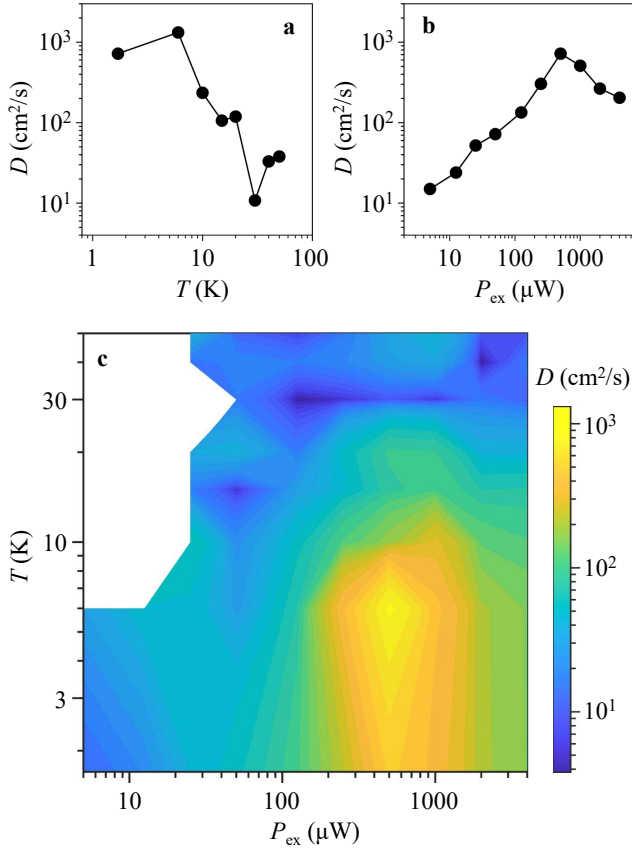


FIG. 3: Temperature and excitation power dependence of IX transport: diffusive transport approach. The IX diffusivity is estimated by least-squares fit of the kinetics of exciton cloud expansion  $\bar{d}_{1/e}(t)$  simulated with Eq. 1 to the measured  $d_{1/e}(t)$  (Fig. 2a). (a-c) The estimated IX diffusivity  $D$  vs. temperature (a), excitation power (b), and temperature and excitation power (c).  $P_{\text{ex}} = 0.5$  mW (a),  $T = 1.7$  K (b).

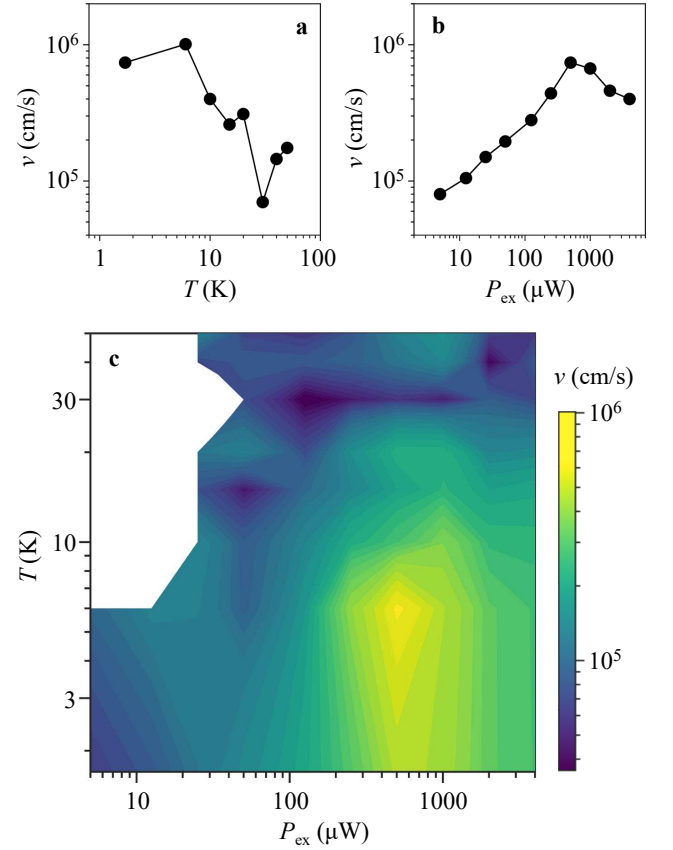


FIG. 4: Temperature and excitation power dependence of IX transport: ballistic transport approach. The IX velocity is estimated by least-squares fit of the kinetics of exciton cloud expansion  $d_{1/e}(t)$  simulated with Eq. 2 to the measured  $d_{1/e}(t)$  (Fig. 2b). (a-c) The estimated IX velocity  $v$  vs. temperature (a), excitation power (b), and temperature and excitation power (c).  $P_{\text{ex}} = 0.5$  mW (a),  $T = 1.7$  K (b).

up to  $D \sim 0.1$  cm<sup>2</sup>/s in Refs. [52, 53] and up to  $D \sim 2$  cm<sup>2</sup>/s in Ref. [55]. The anomalously high diffusivity indicates the anomalously high mean free time  $\tau_m \propto D$ . In turn, the mean free path  $l_m \propto \tau_m$  and, for the high  $D \sim 10^3$  cm<sup>2</sup>/s in the experiment (Fig. 3), the estimated  $l_m$  become anomalously high, as outlined in SI. IXs move with no scattering over the range  $\sim l_m$  and the high  $l_m$  indicate IX long-range ballistic transport.

*Deviation of IX transport from diffusive and ballistic transport.* We compared the deviation of the measured IX transport from the simulated diffusive transport (Fig. 2a) and the simulated ballistic transport (Fig. 2b). The deviation is quantified by  $\chi^2 = \sum (m_i - s_i)^2 / (v s_i)$ , where  $m_i$  and  $s_i$  are the measured and simulated IX cloud extension  $d_{1/e}$  at time  $t$  and  $v$  is the number of the measured  $t$  values in  $\chi^2$  (Fig. 5). In the regime of the efficient IX transport (yellow region in Figs. 3c, 4c),  $\chi^2$  are large for the diffusive transport (Fig. 5a,b,c) and substantially smaller for the ballistic transport (Fig. 5a,b,d). That shows that the

efficient IX transport significantly deviates from the diffusive transport and agrees with the ballistic transport.

This  $\chi^2$  test justifies the same conclusion, which can be made by the eye comparison of the measured and simulated  $d_{1/e}(t)$  in Fig. 2: The data show a strong deviation of the measured efficient IX transport from diffusive transport (the blue dots strongly deviate from the blue line in Fig. 2a) and significantly smaller deviation of the measured efficient IX transport from ballistic transport (the deviation of the blue dots from the blue line in Fig. 2b is significantly smaller).

*Comparison of IX transport with diffusive transport.* For diffusive IX transport in the HS in-plane disorder potential, the diffusivity increases both with temperature, due to IX delocalization from local minima of the disorder potential, and with density, due to IX screening of the disorder potential [9, 12, 67]. However, for the efficient IX transport with the anomalously high  $D$ ,  $\tau_m$ , and  $l_m$ , a different behavior is observed: the diffusivity drops

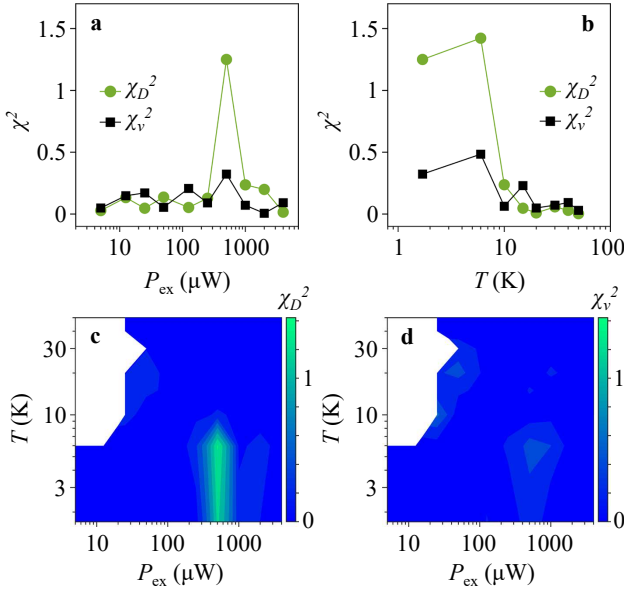


FIG. 5: Comparison of IX transport with diffusive and ballistic transport. (a-d) The deviation of the measured IX transport kinetics from the simulated kinetics  $\chi^2 = \Sigma(m_i - s_i)^2 / (v s_i)$  vs excitation power (a), temperature (b), and excitation power and temperature (c,d).  $m_i$  and  $s_i$  are the measured and simulated IX cloud extension  $d_{1/e}$  at time  $t$  and  $v$  is the number of the measured  $t$  values in  $\chi^2$ . (a,b) Green points (black squares) show  $\chi^2$  deviation of the measured IX transport from the diffusive (ballistic) transport. (c,d)  $\chi^2$  deviation of the measured IX transport from the diffusive (c) and ballistic (d) transport. In the regime of the efficient IX transport (yellow region in Figs. 3c, 4c),  $\chi^2$  are large for the diffusive transport and significantly smaller for the ballistic transport. This shows that the efficient IX transport substantially deviates from the diffusive transport and agrees with the ballistic transport.  $T = 1.7$  K (a),  $P_{\text{ex}} = 0.5$  mW (b).

with temperature and drops with density at high densities (Fig. 3), indicating that the efficient IX transport is inconsistent with the diffusive transport.

Furthermore, both the estimated amplitude of the moiré potential [32–36], and the disorder amplitude,  $\sim 10$  meV, estimated from the PL linewidth (see SI), are high. They are significantly higher than the thermal energy at the temperatures where the efficient IX transport is observed ( $k_B T \lesssim 1$  meV, Fig. 3) so the IX thermal energy is insufficient for effective IX delocalization from the local minima of the in-plane potential for diffusive IX transport [67]. They are also significantly higher than the IX interaction energy at the densities where the efficient IX transport is observed (the IX energy shift due to the interaction  $\delta E \sim 3$  meV for the efficient IX transport) so the IX interaction energy is insufficient for effective screening of the in-plane potential for diffusive IX transport [12]. The efficient IX transport occurs in spite of the strong in-plane potential.

*Comparison of IX transport with BH theory.* The efficient IX transport with the anomalously high  $D$ ,  $\tau_m$ , and  $l_m$ , in spite of the strong in-plane potential, agrees with the BH theory prediction of superfluidity in moiré superlattices. The BH model predicts the superfluid phase for the number of bosons per lattice site  $N \sim 1/2$  and the insulating phase, such as the Mott insulator and the Bose glass, for  $N \sim 0$  and  $N \sim 1$  [68]. The IX diffusivity enhancement followed by the suppression with density (Fig. 3) qualitatively agree with this prediction of the BH model.

The IX density can be estimated by the mean-field formula for the IX energy shift  $\delta E = 4\pi e^2 d_z n / \epsilon$  [69], where  $d_z \sim 0.6$  nm is the separation between the electron and hole layers and  $\epsilon \sim 7.4$  is the dielectric constant [70]. For the efficient IX transport regime,  $\delta E \sim 3$  meV gives  $n \sim 2 \cdot 10^{11} \text{ cm}^{-2}$ .  $N \sim 1/2$  for this density and the moiré superlattice period  $b = 17$  nm, where  $b \sim a/\delta\theta$  corresponds to the twist angle  $\delta\theta = 1.1^\circ$  that agrees with the angle between MoSe<sub>2</sub> and WSe<sub>2</sub> layers in the HS, see SI ( $a$  is the lattice constant).

The efficient IX transport vanishes above  $T \sim 10$  K (Fig. 3). This also agrees with the BH theory prediction for superfluidity in the moiré potential. The BH theory predicts the critical temperature for superfluidity  $T_c \sim 4\pi N J$  [71].  $T_c \sim 10$  K corresponds to the intersite hopping  $J \sim 1.6$  K and, in turn, the moiré superlattice amplitude  $\sim 8$  meV for  $b \sim 17$  nm [72]. This value is comparable to the moiré potential amplitude for the MoSe<sub>2</sub>/WSe<sub>2</sub> HS with H stacking [32–35] (the stacking determines the IX  $g$ -factor [73] and the measured  $g$ -factor corresponds to H stacking in the MoSe<sub>2</sub>/WSe<sub>2</sub> HS).

The agreement of the efficient IX transport with the ballistic transport (Figs. 2b, 5) is consistent with superfluidity since both the ballistic transport and superfluid transport are characterized by the lack of scattering. The ballistic transport models the transport with no scattering. Other modelling, such as modelling using the Gross-Pitaevskii approach, can also be considered.

The density and temperature range of the efficient IX transport with the anomalously high diffusivity (Fig. 3) is consistent with the density and temperature range for the long-distance IX transport and the IX mediated long-distance spin transport in cw studies of IXs in vdW TMD HS [64, 65]. This indicates that the latter phenomena originate from the high IX diffusivity and long-range ballistic transport.

In summary, we found IX transport with the anomalously high diffusivity, orders of magnitude higher than for regular diffusive exciton transport in van der Waals heterostructures. This efficient IX transport agrees with long-range ballistic transport and is consistent with the Bose-Hubbard theory prediction of superfluid in moiré superlattices.

**Acknowledgements** We thank M.M. Fogler, B. Vermilyea, and A.H. MacDonald for discussions and A.K. Geim for teaching us manufacturing TMD HS. The studies were supported by the Department of Energy, Office of Basic Energy Sciences, under award DE-FG02-07ER46449. The HS manufacturing was supported by NSF Grant 1905478.

## References

- 
- [1] L.V. Keldysh, A.N. Kozlov, Collective properties of excitons in semiconductors, *Sov. Phys. JETP* **27**, 521 (1968).
  - [2] Y.E. Lozovik, V.I. Yudson, A new mechanism for superconductivity: pairing between spatially separated electrons and holes, *Sov. Phys. JETP* **44**, 389 (1976).
  - [3] A. Zrenner, P. Leeb, J. Schäfler, G. Böhm, G. Weimann, J.M. Worlock, L.T. Florez, J.P. Harbison, Indirect excitons in coupled quantum well structures, *Surf. Sci.* **263**, 496 (1992).
  - [4] A.A. High, J.R. Leonard, A.T. Hammack, M.M. Fogler, L.V. Butov, A.V. Kavokin, K.L. Campman, A.C. Gossard, Spontaneous coherence in a cold exciton gas, *Nature* **483**, 584 (2012).
  - [5] M. Hagn, A. Zrenner, G. Böhm, G. Weimann, Electric-field-induced exciton transport in coupled quantum well structures, *Appl. Phys. Lett.* **67**, 232 (1995).
  - [6] A.V. Larionov, V.B. Timofeev, J. Hvam, K. Soerensen, Interwell Excitons in GaAs/AlGaAs Double Quantum Wells and Their Collective Properties, *J. Exp. Theor. Phys.* **90**, 1093 (2000).
  - [7] L.V. Butov, A.C. Gossard, D.S. Chemla, Macroscopically ordered state in an exciton system, *Nature* **418**, 751 (2002).
  - [8] Z. Vörös, R. Balili, D.W. Snoke, L. Pfeiffer, K. West, Long-Distance Diffusion of Excitons in Double Quantum Well Structures, *Phys. Rev. Lett.* **94**, 226401 (2005).
  - [9] A.L. Ivanov, L.E. Smallwood, A.T. Hammack, Sen Yang, L.V. Butov, A.C. Gossard, Origin of the inner ring in photoluminescence patterns of quantum well excitons, *Europhys. Lett.* **73**, 920 (2006).
  - [10] A. Gärtner, A.W. Holleitner, J.P. Kotthaus, D. Schuh, Drift mobility of long-living excitons in coupled GaAs quantum wells, *Appl. Phys. Lett.* **89**, 052108 (2006).
  - [11] A.A. High, E.E. Novitskaya, L.V. Butov, M. Hanson, A.C. Gossard, Control of exciton fluxes in an excitonic integrated circuit, *Science* **321**, 229 (2008).
  - [12] M. Remeika, J.C. Graves, A.T. Hammack, A.D. Meyert-holen, M.M. Fogler, L.V. Butov, M. Hanson, A.C. Gossard, Localization-Delocalization Transition of Indirect Excitons in Lateral Electrostatic Lattices, *Phys. Rev. Lett.* **102**, 186803 (2009).
  - [13] X.P. Vögele, D. Schuh, W. Wegscheider, J.P. Kotthaus, A.W. Holleitner, Density Enhanced Diffusion of Dipolar Excitons within a One-Dimensional Channel, *Phys. Rev. Lett.* **103**, 126402 (2009).
  - [14] S. Lazić, P.V. Santos, R. Hey, Exciton transport by moving strain dots in GaAs quantum wells, *Phys. E* **42**, 2640 (2010).
  - [15] M. Alloing, A. Lemaître, E. Galopin, F. Dubin, Nonlinear dynamics and inner-ring photoluminescence pattern of indirect excitons, *Phys. Rev. B* **85**, 245106 (2012).
  - [16] A.A. High, A.T. Hammack, J.R. Leonard, Sen Yang, L.V. Butov, T. Ostatnický, M. Vladimirova, A.V. Kavokin, T.C.H. Liew, K.L. Campman, A.C. Gossard, Spin Currents in a Coherent Exciton Gas, *Phys. Rev. Lett.* **110**, 246403 (2013).
  - [17] S. Lazić, A. Violante, K. Cohen, R. Hey, R. Rapaport, P.V. Santos, Scalable interconnections for remote indirect exciton systems based on acoustic transport, *Phys. Rev. B* **89**, 085313 (2014).
  - [18] Mathieu Alloing, Mussie Beian, Maciej Lewenstein, David Fuster, Yolanda González, Luisa González, Roland Combescot, Monique Combescot, François Dubin, Evidence for a Bose-Einstein condensate of excitons, *Europhys. Lett.* **107**, 10012 (2014).
  - [19] A.V. Gorbunov, V.B. Timofeev, Coherence of Bose-Einstein condensates of dipolar excitons in GaAs/AlGaAs heterostructures, *Low. Temp. Phys.* **42**, 340 (2016).
  - [20] J.R. Leonard, A.A. High, A.T. Hammack, M.M. Fogler, L.V. Butov, K.L. Campman, A.C. Gossard, Pancharatnam-Berry phase in condensate of indirect excitons, *Nat. Commun.* **9**, 2158 (2018).
  - [21] J.R. Leonard, Lunhui Hu, A.A. High, A.T. Hammack, Congjun Wu, L.V. Butov, K.L. Campman, A.C. Gossard, Moiré pattern of interference dislocations in condensate of indirect excitons, *Nat. Commun.* **12**, 1175 (2021).
  - [22] François Chiaruttini, Thierry Guillet, Christelle Brimont, Benoit Jouault, Pierre Lefebvre, Jessica Vives, Sebastien Chenot, Yvon Cordier, Benjamin Damilano, Maria Vladimirova, Trapping Dipolar Exciton Fluids in GaN/(AlGa)N Nanostructures, *Nano Lett.* **19**, 4911 (2019).
  - [23] Y.Y. Kuznetsova, F. Fedichkin, P. Andreakou, E.V. Calman, L.V. Butov, P. Lefebvre, T. Bretagnon, T. Guillet, M. Vladimirova, C. Morhain, J.-M. Chauveau, Transport of indirect excitons in ZnO quantum wells, *Opt. Lett.* **40**, 3667 (2015).
  - [24] Ziliang Ye, Ting Cao, Kevin O'Brien, Hanyu Zhu, Xiaobo Yin, Yuan Wang, Steven G. Louie, Xiang Zhang, Probing excitonic dark states in single-layer tungsten disulphide, *Nature* **513**, 214 (2014).
  - [25] Alexey Chernikov, Timothy C. Berkelbach, Heather M. Hill, Albert Rigosi, Yilei Li, Ozgur Burak Aslan, David R. Reichman, Mark S. Hybertsen, Tony F. Heinz, Exciton Binding Energy and Nonhydrogenic Rydberg Series in Monolayer WS<sub>2</sub>, *Phys. Rev. Lett.* **113**, 076802 (2014).
  - [26] M. Goryca, J. Li, A.V. Stier, T. Taniguchi, K. Watanabe, E. Courtade, S. Shree, C. Robert, B. Urbaszek, X. Marie, S.A. Crooker, Revealing exciton masses and dielectric properties of monolayer semiconductors with high magnetic fields, *Nat. Commun.* **10**, 4172 (2019).
  - [27] M.M. Fogler, L.V. Butov, K.S. Novoselov, High-temperature superfluidity with indirect excitons in van der Waals heterostructures, *Nat. Commun.* **5**, 4555 (2014).
  - [28] Thorsten Deilmann, Kristian Sommer Thygesen, Inter-layer Trions in the MoS<sub>2</sub>/WS<sub>2</sub> van der Waals Heterostructure, *Nano Lett.* **18**, 1460 (2018).
  - [29] K. Sivalertporn, L. Mouchliadis, A.L. Ivanov, R. Philp, E.A. Muljarov, Direct and indirect excitons in semiconductor coupled quantum wells in an applied electric field, *Phys. Rev. B* **85**, 045207 (2012).
  - [30] Erik A. Szwed, Brian Vermilyea, Darius J. Choksy, Zhiwen Zhou, Michael M. Fogler, Leonid V. Butov,



- Dmitry K. Efimkin, Kirk W. Baldwin, Loren Pfeiffer, Excitonic Bose Polarons in Electron-Hole Bilayers, *Nano Lett.* **24**, 13219 (2024).
- [31] C. Morhain, T. Bretagnon, P. Lefebvre, X. Tang, P. Valvin, T. Guillet, B. Gil, T. Taliercio, M. Teisseire-Doninelli, B. Vinter, C. Deparis, Internal electric field in wurtzite  $\text{ZnO}/\text{Zn}_{0.78}\text{Mg}_{0.22}\text{O}$  quantum wells, *Phys. Rev. B* **72**, 241305(R) (2005).
- [32] Fengcheng Wu, Timothy Lovorn, A.H. MacDonald, Theory of optical absorption by interlayer excitons in transition metal dichalcogenide heterobilayers, *Phys. Rev. B* **97**, 035306 (2018).
- [33] Hongyi Yu, Gui-Bin Liu, Wang Yao, Brightened spin-triplet interlayer excitons and optical selection rules in van der Waals heterobilayers, *2D Mater.* **5**, 035021 (2018).
- [34] Fengcheng Wu, Timothy Lovorn, A.H. MacDonald, Topological Exciton Bands in Moiré Heterojunctions, *Phys. Rev. Lett.* **118**, 147401 (2017).
- [35] Hongyi Yu, Gui-Bin Liu, Jianju Tang, Xiaodong Xu, Wang Yao, Moiré excitons: From programmable quantum emitter arrays to spin-orbit-coupled artificial lattices, *Sci. Adv.* **3**, e1701696 (2017).
- [36] Chendong Zhang, Chih-Piao Chuu, Xibiao Ren, Ming-Yang Li, Lain-Jong Li, Chuanhong Jin, Mei-Yin Chou, Chih-Kang Shih, Interlayer couplings, Moiré patterns, and 2D electronic superlattices in  $\text{MoS}_2/\text{WSe}_2$  hetero-bilayers, *Sci. Adv.* **3**, e1601459 (2017).
- [37] Nardeep Kumar, Qiannan Cui, Frank Ceballos, Dawei He, Yongsheng Wang, Hui Zhao, Exciton diffusion in monolayer and bulk  $\text{MoSe}_2$ , *Nanoscale* **6**, 4915, (2014).
- [38] Marvin Kulig, Jonas Zipfel, Philipp Nagler, Sofia Blanter, Christian Schüller, Tobias Korn, Nicola Paradiso, Mikhail M. Glazov, Alexey Chernikov, Exciton Diffusion and Halo Effects in Monolayer Semiconductors, *Phys. Rev. Lett.* **120**, 207401 (2018).
- [39] F. Cadiz, C. Robert, E. Courtade, M. Manca, L. Martinelli, T. Taniguchi, K. Watanabe, T. Amand, A.C.H. Rowe, D. Paget, B. Urbaszek, X. Marie, Exciton diffusion in  $\text{WSe}_2$  monolayers embedded in a van der Waals heterostructure, *Appl. Phys. Lett.* **112**, 152106 (2018).
- [40] Darwin F. Cordovilla Leon, Zidong Li, Sung Woon Jang, Che-Hsuan Cheng, Parag B. Deotare, Exciton transport in strained monolayer  $\text{WSe}_2$ , *Appl. Phys. Lett.* **113**, 252101 (2018).
- [41] Darwin F. Cordovilla Leon, Zidong Li, Sung Woon Jang, Parag B. Deotare, Hot exciton transport in  $\text{WSe}_2$  monolayers, *Phys. Rev. B* **100**, 241401(R) (2019).
- [42] Shengcai Hao, Matthew Z. Bellus, Dawei He, Yongsheng Wang, Hui Zhao, Controlling exciton transport in monolayer  $\text{MoSe}_2$  by dielectric screening, *Nanoscale Horiz.* **5**, 139 (2020).
- [43] Kanak Datta, Zhengyang Lyu, Zidong Li, Takashi Taniguchi, Kenji Watanabe, Parag B. Deotare, Spatiotemporally controlled room-temperature exciton transport under dynamic strain, *Nat. Photonics* **16**, 242 (2022).
- [44] Pasqual Rivera, Kyle L. Seyler, Hongyi Yu, John R. Schaibley, Jiaqiang Yan, David G. Mandrus, Wang Yao, Xiaodong Xu, Valley-polarized exciton dynamics in a 2D semiconductor heterostructure, *Science* **351**, 688 (2016).
- [45] Luis A. Jauregui, Andrew Y. Joe, Katerina Pistunova, Dominik S. Wild, Alexander A. High, You Zhou, Giovanni Scuri, Kristiaan De Greve, Andrey Sushko, Che-Hang Yu, Takashi Taniguchi, Kenji Watanabe, Daniel J. Needleman, Mikhail D. Lukin, Hongkun Park, Philip Kim, Electrical control of interlayer exciton dynamics in atomically thin heterostructures, *Science* **366**, 870 (2019).
- [46] Dmitrii Unuchek, Alberto Ciarrocchi, Ahmet Avsar, Kenji Watanabe, Takashi Taniguchi, Andras Kis, Room-temperature electrical control of exciton flux in a van der Waals heterostructure, *Nature* **560**, 340 (2019).
- [47] Dmitrii Unuchek, Alberto Ciarrocchi, Ahmet Avsar, Zhe Sun, Kenji Watanabe, Takashi Taniguchi, Andras Kis, Valley-polarized exciton currents in a van der Waals heterostructure, *Nat. Nanotechnol.* **14**, 1104 (2019).
- [48] Yuanda Liu, Kevin Dini, Qinghai Tan, Timothy Liew, Kostya S. Novoselov, Weibo Gao, Electrically controllable router of interlayer excitons, *Sci. Adv.* **6**, eaba1830 (2020).
- [49] Junho Choi, Wei-Ting Hsu, Li-Syuan Lu, Liuyang Sun, Hui-Yu Cheng, Ming-Hao Lee, Jiamin Quan, Kha Tran, Chun-Yuan Wang, Matthew Staab, Kayleigh Jones, Takashi Taniguchi, Kenji Watanabe, Ming-Wen Chu, Shangji Gwo, Suenne Kim, Chih-Kang Shih, Xiaoqin Li, Wen-Hao Chang, Moiré potential impedes interlayer exciton diffusion in van der Waals heterostructures, *Sci. Adv.* **6**, eaba8866 (2020).
- [50] Zumeng Huang, Yuanda Liu, Kevin Dini, Qinghai Tan, Zhuojun Liu, Hanlin Fang, Jin Liu, Timothy Liew, Weibo Gao, Robust room temperature valley Hall effect of interlayer excitons, *Nano Lett.* **20**, 1345 (2020).
- [51] Long Yuan, Biyuan Zheng, Jens Kunstmann, Thomas Brumme, Agnieszka Beata Kuc, Chao Ma, Shibin Deng, Daria Blach, Anlian Pan, Libai Huang, Twist-angle-dependent interlayer exciton diffusion in  $\text{WS}_2\text{-WSe}_2$  heterobilayers, *Nat. Mater.* **19**, 617 (2020).
- [52] Zidong Li, Xiaobo Lu, Darwin F. Cordovilla Leon, Zhengyang Lyu, Hongchao Xie, Jize Hou, Yanzhao Lu, Xiaoyu Guo, Austin Kaczmarek, Takashi Taniguchi, Kenji Watanabe, Liuyan Zhao, Li Yang, Parag B. Deotare, Interlayer Exciton Transport in  $\text{MoSe}_2/\text{WSe}_2$  Heterostructures, *ACS Nano* **15**, 1539 (2021).
- [53] Jue Wang, Qianhui Shi, En-Min Shih, Lin Zhou, Wenjing Wu, Yusong Bai, Daniel Rhodes, Katayun Barmak, James Hone, Cory R. Dean, X.-Y. Zhu, Diffusivity Reveals Three Distinct Phases of Interlayer Excitons in  $\text{MoSe}_2/\text{WSe}_2$  Heterobilayers, *Phys. Rev. Lett.* **126**, 106804 (2021).
- [54] Daniel N. Shanks, Fateme Mahdikhany Sarvejahany, Trevor G. Stanfill, Michael R. Koehler, David G. Mandrus, Takashi Taniguchi, Kenji Watanabe, Brian J. LeRoy, John R. Schaibley, Interlayer Exciton Diode and Transistor, *Nano Lett.* **22**, 6599 (2022).
- [55] Zhe Sun, Alberto Ciarrocchi, Fedele Tagarelli, Juan Francisco Gonzalez Marin, Kenji Watanabe, Takashi Taniguchi, Andras Kis, Excitonic transport driven by repulsive dipolar interaction in a van der Waals heterostructure, *Nat. Photonics* **16**, 79 (2022).
- [56] Fedele Tagarelli, Edoardo Lopriore, Daniel Erkensten, Raúl Perea-Causín, Samuel Brem, Joakim Hagel, Zhe Sun, Gabriele Pasquale, Kenji Watanabe, Takashi Taniguchi, Ermin Malic, Andras Kis, Electrical control of hybrid exciton transport in a van der Waals heterostructure, *Nat. Photonics* **17**, 615 (2023).
- [57] Antonio Rossi, Jonas Zipfel, Indrajit Maity, Monica Lorenzon, Luca Francaviglia, Emma C. Regan, Zuocheng Zhang, Jacob H. Nie, Edward Barnard, Kenji Watanabe, Takashi Taniguchi, Eli Rotenberg, Feng Wang, Johannes Lischner, Archana Raja, Alexander Weber-Bargioni, Phason-mediated interlayer exciton diffusion in  $\text{WS}_2/\text{WSe}_2$  moiré heterostructure, arXiv:2301.07750 (2023).

- [58] Beini Gao, Daniel G. Suárez-Forero, Supratik Sarkar, Tsung-Sheng Huang, Deric Session, Mahmoud Jalali Mehrabad, Ruihao Ni, Ming Xie, Pranshoo Upadhyay, Jonathan Vannucci, Sunil Mittal, Kenji Watanabe, Takashi Taniguchi, Atac Imamoglu, You Zhou, Mohammad Hafezi, Excitonic Mott insulator in a Bose-Fermi-Hubbard system of moiré  $\text{WS}_2/\text{WSe}_2$  heterobilayer, *Nat. Commun.* **15**, 2305 (2024).
- [59] Lifu Zhang, Liuxin Gu, Ruihao Ni, Ming Xie, Suji Park, Houk Jang, Rundong Ma, Takashi Taniguchi, Kenji Watanabe, You Zhou, Electrical Control and Transport of Tightly Bound Interlayer Excitons in a  $\text{MoSe}_2/\text{hBN}/\text{MoSe}_2$  Heterostructure, *Phys. Rev. Lett.* **132**, 216903 (2024).
- [60] L.H. Fowler-Gerace, D.J. Choksy, L.V. Butov, Voltage-controlled long-range propagation of indirect excitons in a van der Waals heterostructure, *Phys. Rev. B* **104**, 165302 (2021).
- [61] Ruoming Peng, Adina Ripin, Yusen Ye, Jiayi Zhu, Changming Wu, Seokhyeong Lee, Huan Li, Takashi Taniguchi, Kenji Watanabe, Ting Cao, Xiaodong Xu, Mo Li, Long-range transport of 2D excitons with acoustic waves, *Nat. Commun.* **13**, 1334 (2022).
- [62] Mirco Troue, Johannes Figueiredo, Lukas Sigl, Christos Paspalides, Manuel Katzer, Takashi Taniguchi, Kenji Watanabe, Malte Selig, Andreas Knorr, Ursula Wurstbauer, Alexander W. Holleitner, Extended Spatial Coherence of Interlayer Excitons in  $\text{MoSe}_2/\text{WSe}_2$  Heterobilayers, *Phys. Rev. Lett.* **131**, 036902 (2023).
- [63] Jacob Cutshall, Fateme Mahdikhany, Anna Roche, Daniel N. Shanks, Michael R. Koehler, David G. Mandrus, Takashi Taniguchi, Kenji Watanabe, Qizhong Zhu, Brian J. LeRoy, John R. Schaibley, Imaging interlayer exciton superfluidity in a 2D semiconductor heterostructure, *Sci. Adv.* **11**, eadr1772 (2025).
- [64] L.H. Fowler-Gerace, Zhiwen Zhou, E.A. Szwed, D.J. Choksy, L.V. Butov, Transport and localization of indirect excitons in a van der Waals heterostructure, *Nat. Photonics* **18**, 823 (2024).
- [65] Zhiwen Zhou, E.A. Szwed, D.J. Choksy, L.H. Fowler-Gerace, L.V. Butov, Long-distance decay-less spin transport in indirect excitons in a van der Waals heterostructure, *Nat. Commun.* **15**, 9454 (2024).
- [66] Pasqual Rivera, John R. Schaibley, Aaron M. Jones, Jason S. Ross, Sanfeng Wu, Grant Aivazian, Philip Klement, Kyle Seyler, Genevieve Clark, Nirmal J. Ghimire, Jiaqiang Yan, D.G. Mandrus, Wang Yao, Xiaodong Xu, Observation of long-lived interlayer excitons in monolayer  $\text{MoSe}_2$ - $\text{WSe}_2$  heterostructures, *Nat. Commun.* **6**, 6242 (2015).
- [67] A.L. Ivanov, Quantum diffusion of dipole-oriented indirect excitons in coupled quantum wells, *Europhys. Lett.* **59**, 586 (2002).
- [68] Matthew P. A. Fisher, Peter B. Weichman, G. Grinstein, Daniel S. Fisher, Boson localization and the superfuid-insulator transition, *Phys. Rev. B* **40**, 546 (1989).
- [69] Daijiro Yoshioka, Allan H. MacDonald, Double quantum well electron-hole systems in strong magnetic fields. *J. Phys. Soc. Jpn.* **59**, 4211 (1990).
- [70] Akash Laturia, Maarten L. Van de Put, William G. Vandenberghe, Dielectric properties of hexagonal boron nitride and transition metal dichalcogenides: from monolayer to bulk, *npj 2D Mater. Appl.* **2**, 6 (2018).
- [71] Barbara Capogrosso-Sansone, Şebnem Güneş Söyler, Nikolay Prokof'ev, Boris Svistunov, Monte Carlo study of the two-dimensional Bose-Hubbard model, *Phys. Rev. A* **77**, 015602 (2008).
- [72] M. Remeika, M.M. Fogler, L.V. Butov, M. Hanson, A.C. Gossard, Two-dimensional electrostatic lattices for indirect excitons, *Appl. Phys. Lett.* **100**, 061103 (2012).
- [73] Tomasz Woźniak, Paulo E. Faria Junior, Gotthard Seifert, Andrey Chaves, Jens Kunstmann, Exciton  $g$  factors of van der Waals heterostructures from first-principles calculations, *Phys. Rev. B* **101**, 235408 (2020).

# Supporting Information for Efficient transport of indirect excitons in a van der Waals heterostructure

Zhiwen Zhou,<sup>1</sup> W. J. Brunner,<sup>1</sup> E. A. Szwed,<sup>1</sup> H. Henstridge,<sup>1</sup> L. H. Fowler-Gerace,<sup>1</sup> and L. V. Butov<sup>1</sup>

<sup>1</sup>Department of Physics, University of California San Diego, La Jolla, CA 92093, USA

(Dated: July 8, 2025)

## Heterostructure

The vdW MoSe<sub>2</sub>/WSe<sub>2</sub> HS (Fig. S1a) was assembled using the dry-transfer peel technique [1]. The HS manufacturing details are described in Ref. [2], where the same HS was used for cw studies of IXs. The thickness of the bottom hBN layer is  $\sim 40$  nm, the thickness of the top hBN layer is  $\sim 30$  nm. The MoSe<sub>2</sub> monolayer is on top of the WSe<sub>2</sub> monolayer. The WSe<sub>2</sub> and MoSe<sub>2</sub> edges reach  $\sim 30$  and  $\sim 20$   $\mu\text{m}$ , respectively, (Fig. S1b) that enables a rotational alignment between the WSe<sub>2</sub> and MoSe<sub>2</sub> monolayers. The twist angle between the monolayers  $\delta\theta = 1.1^\circ$  corresponding to the moiré superlattice period  $b = 17$  nm agrees with the angle between MoSe<sub>2</sub> and WSe<sub>2</sub> edges in the HS (Fig. S1b).

The accuracies of estimating  $\delta\theta$  using the long WSe<sub>2</sub> and MoSe<sub>2</sub> edges and using SHG are comparable. We do not use SHG for additional estimates of  $\delta\theta$  since the intense excitation pulses in SHG measurements may cause a deterioration of the HS and may suppress the efficient IX transport. The moiré potentials can be affected by atomic reconstruction [3–5] and by disorder and may vary over the HS area.

The IX  $g$ -factor is determined by the HS stacking [6]. The measured  $g$ -factor corresponds to H stacking in the MoSe<sub>2</sub>/WSe<sub>2</sub> HS.

Figure S1b presents a microscope image showing the layer pattern of the HS. The layer boundaries are indicated. The hBN layers cover the entire areas of MoSe<sub>2</sub> and WSe<sub>2</sub> layers. There was a narrow multilayer graphene electrode on the top of the HS around  $x = 2$   $\mu\text{m}$  for  $y = 0$  in Fig. S1b. This electrode was detached.

So far, the efficient IX transport in vdW TMD HS was realized in one sample in this work. Other samples in other studies of vdW TMD heterostructures show diffusive IX transport with significantly smaller diffusivities as outlined in the main text. The smaller diffusivity likely originates from stronger disorder, which causes IX scattering and localization. When disorder is large it breaks exciton superfluidity. With lowering the disorder, superfluidity first emerges in small disconnected puddles, then the puddles grow in size, and for the low disorder superfluid percolating through the entire sample emerges. This leads to non-diffusive efficient IX transport through the entire vdW TMD HS. This work demonstrates the existence of the efficient IX transport in TMD heterostructures. It is essential to study this phenomenon in other samples with different HS parameters. However, the sample statistics of other IX transport studies in vdW TMD heterostructures outlined in the main text shows that it is challenging to manufacture samples with different HS parameters, all with sufficiently small disorder. This is the subject for future works.

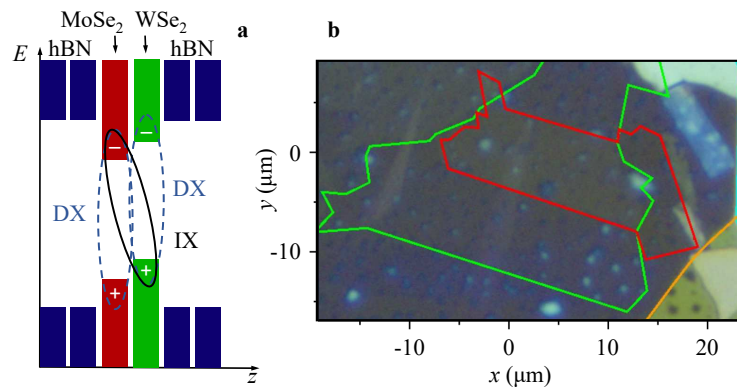


FIG. S1: (a) Schematic energy-band diagram of the MoSe<sub>2</sub>/WSe<sub>2</sub> vdW HS. The ovals indicate DXs and IX composed of an electron (–) and a hole (+). (b) A microscope image showing the HS layers. The green, red, cyan, and orange lines indicate the boundaries of WSe<sub>2</sub> and MoSe<sub>2</sub> monolayers and bottom and top hBN layers, respectively.



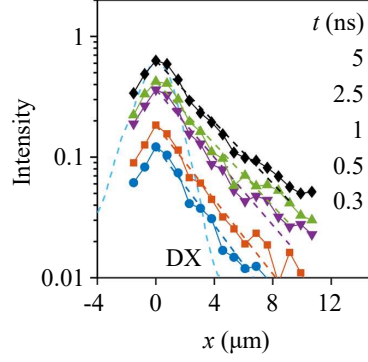


FIG. S2: IX PL spatial profiles  $I(x)$  vs. time  $t$  after the start of laser excitation pulse. IXs are created by the laser excitation. The excitation spot is centered at  $x = 0$  and is shown by cyan dotted line that presents the DX PL profile in WSe<sub>2</sub> monolayer and is close to the laser profile for short-range DX transport. The dashed lines show least-squares exponential fits to the decays of the IX cloud profiles  $I(x, t)$  to exponential decays in the region from the excitation spot to the HS edge,  $x = 0 - 9 \mu\text{m}$ .  $P_{\text{ex}} = 0.5 \text{ mW}$ ,  $T = 50 \text{ K}$ . The IX cloud expands and the  $1/e$  decay distance of the IX cloud  $d_{1/e}$  increases with time due to IX transport. In contrast to the data in Fig. 1a in the main text presenting  $I(x, t)$  for the efficient IX transport, the enhancement of  $d_{1/e}$  with time in Fig. S2 is significantly slower that corresponds to significantly lower IX diffusivity at these parameters. The range of parameters of the efficient IX transport with the anomalously high diffusivity is presented in Fig. 3 in the main text.

### Optical measurements

Excitons were generated by a semiconductor laser with the excitation energy  $E_{\text{ex}} = 1.689 \text{ eV}$  resonant to DX in WSe<sub>2</sub> HS layer. The laser pulses had step-like rectangular shape with 80 ns pulse width, 0.1 ns pulse rise time, 0.3 ns pulse fall time (the pulses rise and fall  $e$  times within 0.1 and 0.3 ns, respectively), and 300 ns pulse period. The 220 ns off time exceeded the IX lifetime (Fig. S3) and was sufficient for a substantial decay of the IX signal.

The IX transport was measured by time- and spatially-resolved optical imaging using an avalanche photodiode (APD). The APD was moved in the plane of the optical image to measure the IX PL kinetics  $I(x, t)$ . For the image magnification  $\times 92$  and the APD window diameter  $100 \mu\text{m}$ , the spatial integration of the imaging setup  $\sim 1.1 \mu\text{m}$  was substantially smaller than the IX transport distances (Fig. 1 in the main text). The APD time resolution was 0.1 ns. Both the spatial and time resolution of the time-resolve imaging setup was sufficient for the time-resolved imaging of the IX transport. The IX emission in the time-resolved imaging experiments was spectrally selected by the long-pass filter with cut-off wavelength 850 nm (1.459 eV).

PL spectra (Fig. S7) were measured using a spectrometer with a resolution of 0.2 meV and a liquid-nitrogen-cooled charge-coupled device. The experiments were performed in a variable-temperature 4He cryostat. The sample was mounted on an Attocube  $xyz$  piezo translation stage allowing adjusting the sample position relative to a focusing lens inside the cryostat. All phenomena presented in this work are reproducible after multiple cooling down to 2 K and warming up to room temperature.

### Spatial profiles $I(x, t)$

A representative example of IX cloud expansion with time  $I(x, t)$  in the regime of efficient IX transport is presented in Fig. 1a in the main text. Figure S2 shows a representative example of  $I(x, t)$  in the regime of regular diffusive IX transport. In contrast to the efficient IX transport with the fast enhancement of the spatial extension of IX cloud  $d_{1/e}(t)$  with time (Fig. 1a in the main text), for the regular diffusive IX transport the enhancement of  $d_{1/e}(t)$  with time is significantly slower (Fig. S2). The difference between the regime of the non-diffusive efficient IX transport regime and the diffusive transport regime is quantified by the anomalously high IX diffusivity for the former and is outlined in the main text.

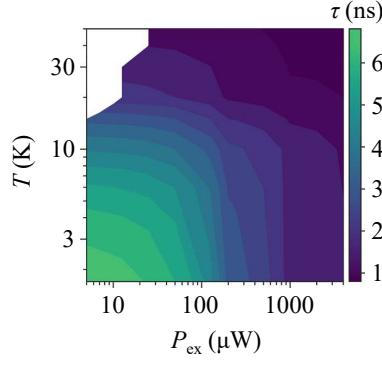


FIG. S3: The IX recombination lifetime  $\tau$  vs. excitation power  $P_{\text{ex}}$  and temperature  $T$ .  $\tau$  is the initial decay time after the excitation pulse end.

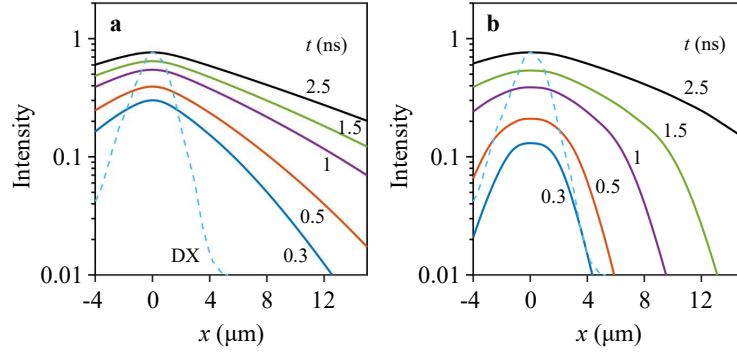


FIG. S4: Simulated spatial profiles  $I(x, t)$  for diffusive (a) and ballistic (b) IX transport using, respectively, Eq. 1 and Eq. 2 in the main text. For these simulations, the IX diffusivity  $D = 720 \text{ cm}^2/\text{s}$  in (a), the IX velocity  $v = 7.4 \cdot 10^5 \text{ cm/s}$  in (b), and the IX lifetime  $\tau = 2.7 \text{ ns}$  in (a,b). The dotted lines show the spatial profile of the laser excitation spot  $\Lambda(x)$ . The excitation pulse starts at  $t = 0$ .

### Lifetime

The IX recombination lifetime  $\tau$  was estimated from the measurements of the decay kinetics of the spatially integrated IX signal after the excitation pulse end. The spatial integration minimizes the effect of IX transport on the measured kinetics and realizes the regime where the decay kinetics is governed by the IX recombination. We probed excitation pulse widths from 5 to 80 ns, the variation of  $\tau$  for different pulse widths was small. Both increasing excitation power and temperature led to a reduction of  $\tau$  (Fig. S3). These variations of  $\tau$  were included in the simulations using Eqs. 1 and 2 outlined in the main text, where the measured values of  $\tau(P_{\text{ex}}, T)$  were used.

### Simulated spatial profiles $I(x, t)$

Examples of simulated spatial profiles  $I(x, t)$  for diffusive and ballistic IX transport using, respectively, Eq. 1 and Eq. 2 in the main text are shown in Fig. S4. The simulations used the spatial profile of the laser excitation spot  $\Lambda(x)$ , given by the measured DX PL profile in WSe<sub>2</sub> monolayer that is close to the laser profile for short-range DX transport, and the IX lifetime  $\tau$  presented in Fig. S3. The simulations were performed using the Crank-Nicolson method for numerically solving the diffusion equation [7].

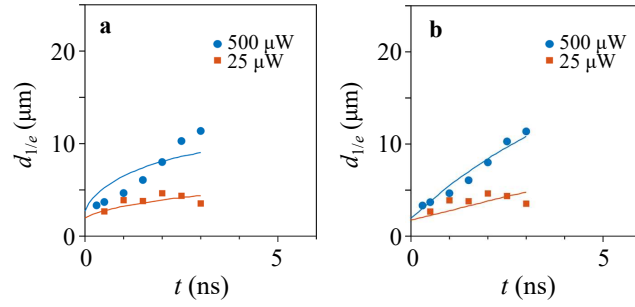


FIG. S5: Simulations of IX cloud expansion. The measured IX cloud expansion  $d_{1/e}(t)$  is shown by blue points for the excitation power  $P_{\text{ex}} = 500 \mu\text{W}$  and by red squares for  $P_{\text{ex}} = 25 \mu\text{W}$ . The simulated  $d_{1/e}(t)$  for diffusive (a) and ballistic (b) IX transport are shown by lines. In the simulations, the IX diffusivity  $D$  for diffusive transport (a) and IX velocity  $v$  for ballistic transport (b) are estimated by least-squares fit of the kinetics of exciton cloud expansion  $d_{1/e}(t)$  simulated with Eq. 1 and Eq. 2 in the main text, respectively, to the measured  $d_{1/e}(t)$ . The simulations in Fig. S5 are similar to the simulations in Fig. 2 in the main text, however, the fit range is  $t = 0 - 3$  ns in Fig. S5 and  $t = 0 - 5$  ns in Fig. 2 in the main text. The estimates for  $D$  and  $v$  obtained with the simulations with the fit range  $t = 0 - 3$  ns (Fig. S5) are presented in Fig. S6. The laser excitation pulse starts at  $t = 0$ .  $T = 1.7$  K.

#### On the analysis of $d_{1/e}(t)$

In the main text, the IX diffusivity  $D$  is estimated by least-squares fit of the kinetics of exciton cloud expansion  $d_{1/e}(t)$  simulated with Eq. 1 to the measured  $d_{1/e}(t)$  in the time range  $t = 0 - 5$  ns (Fig. 2a), and the IX velocity  $v$  is estimated by least-squares fit of the kinetics of exciton cloud expansion  $d_{1/e}(t)$  simulated with Eq. 2 to the measured  $d_{1/e}(t)$  in the time range  $t = 0 - 5$  ns (Fig. 2b). The results are similar for the fits made in different time ranges. Figure S5 shows the fits similar to the fits in Fig. 2 in the main text, however, for the fit range  $t = 0 - 3$  ns. These fits give the values of  $D$  and  $v$  shown in Fig. S6. The fits over  $t = 0 - 3$  ns give similar  $D$  and  $v$  values and their similar temperature and excitation density dependence  $D(P_{\text{ex}}, T)$  and  $v(P_{\text{ex}}, T)$  as the fits over  $t = 0 - 5$  ns in the main text (compare Fig. S6 and Figs. 3 and 4 in the main text). Furthermore, for the efficient IX transport, the fits over  $t = 0 - 3$  ns show a high deviation of the measured  $d_{1/e}(t)$  from diffusive transport (Fig. S5a) and significantly smaller deviation of the measured  $d_{1/e}(t)$  from ballistic transport (Fig. S5b), similarly to the fits over  $t = 0 - 5$  ns as outlined in the main text. The specifics of the fits over  $t = 0 - 3$  ns is that  $d_{1/e}(t)$  in this time range is within the HS area (Fig. S5).

The estimates are obtained using Eqs. 1 and 2 with constant values for  $D$  and  $v$ . During the excitation pulse, the IX density varies with time. Simulations of IX kinetics with density-dependent  $D$  and  $v$  that can improve the accuracy of estimates is the subject of future works.

#### Estimates of IX mean free time and mean free path

IXs are out-of-plane dipoles and repulsive dipolar interaction between IXs can be approximated by the mean-field formula for the IX energy shift with density  $\delta E = nu_0$ ,  $u_0 = 4\pi e^2 d_z / \epsilon$  [ $d_z$  is the separation between the electron and hole layers,  $\epsilon$  is the dielectric constant). The IX interaction introduces interaction-induced drift from the origin and IX transport with the drift can be described as diffusive transport with the enhanced diffusivity  $D = D_0(1 + nu_0/k_B T)$ , where  $D_0$  is the diffusivity for non-interacting particles [9].

The mean free time  $\tau_m$  and the mean free path  $l_m$  can be estimated from  $\tau_m \sim mD_0/(k_B T)$  and  $l_m \sim v\tau_m$ , where the IX mass  $m \sim$  free electron mass for the HS. For the highest  $D \sim 1.3 \cdot 10^3 \text{ cm}^2/\text{s}$  in the experiment (Fig. 3), the estimated mean free time and mean free path reach the anomalously high values:  $\tau_m \sim 0.2$  ns and  $l_m \sim 2 \mu\text{m}$ . The equations for  $\tau_m$  and  $l_m$  in these estimates describe classical diffusive transport regime with short  $l_m$  and small  $v$ . More accurate estimates extended to the parameters of the non-diffusive efficient IX transport regime is the subject of future works.

#### IX PL spectra

Figure S7 shows typical IX spectra. The IX PL linewidth gives an estimate for the disorder amplitude in the HS. Both the smallest IX linewidth at the lowest densities  $\sim 14$  meV and the IX linewidth at the excitation densities

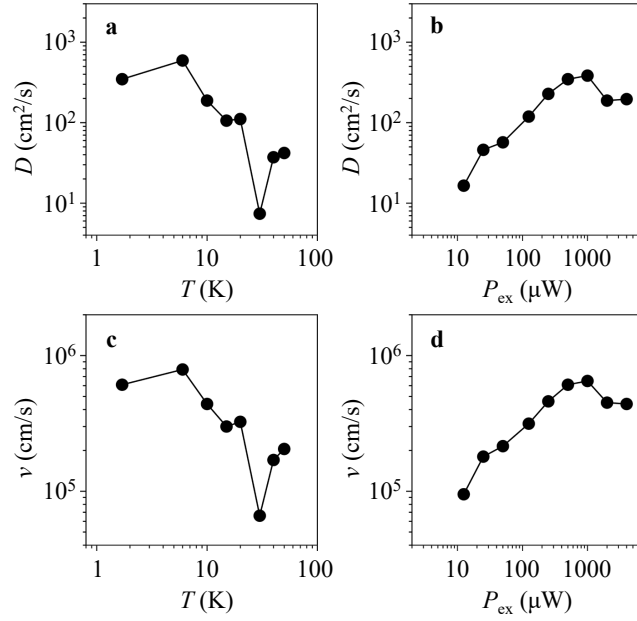


FIG. S6: Temperature and excitation power dependence of IX transport: diffusive transport approach (a,b) and ballistic transport approach (c,d). The IX diffusivity for diffusive transport and IX velocity for ballistic transport are estimated by least-squares fit of the kinetics of exciton cloud expansion  $d_{1/e}(t)$  simulated with Eq. 1 and Eq 2 in the main text, respectively, to the measured  $d_{1/e}(t)$ . The estimates in Fig. S6 are similar to the estimates in Figs. 3, 4 in the main text, however, the fit range is  $t = 0 - 3$  ns in Fig. S6 and  $t = 0 - 5$  ns in Figs. 3, 4 in the main text. (a,b) The estimated IX diffusivity  $D$  vs. temperature (a) and excitation power (b). (c,d) The estimated IX velocity  $v$  vs. temperature (c) and excitation power (d).  $P_{\text{ex}} = 0.5$  mW (a,c),  $T = 1.7$  K (b,d).

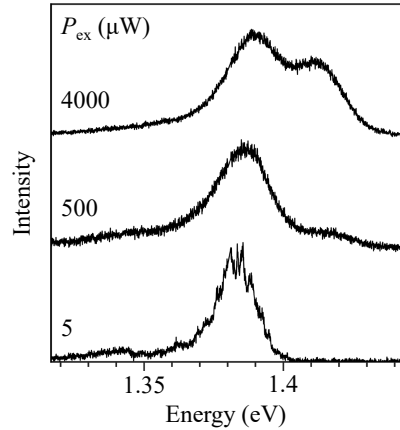


FIG. S7: IX PL spectra at excitation powers  $P_{\text{ex}} = 5, 50$ , and  $4000 \mu\text{W}$  at the excitation spot position.  $T = 1.7$  K.

corresponding to the efficient IX transport  $\sim 20$  meV are significantly larger than the IX interaction energy at the densities where the efficient IX transport is observed  $\sim 3$  meV. Therefore, the IX interaction energy is insufficient for effective screening of the in-plane potential for diffusive IX transport [10]. The non-diffusive efficient IX transport occurs in spite of the strong in-plane potential as outlined in the main text.

Narrow lines appearing in the IX spectrum at lower densities (Fig. S7) were attributed to localized states [11]. A higher-energy IX line appearing at high IX densities (Fig. S7) was attributed to the appearance of moiré cells with double occupancy [11]. The data are spectrally integrated over the entire IX PL and all IX states are included in the transport measurements.

## References

---

- [1] F. Withers, O. Del Pozo-Zamudio, A. Mishchenko, A.P. Rooney, A. Gholinia, K. Watanabe, T. Taniguchi, S.J. Haigh, A.K. Geim, A.I. Tartakovskii, K.S. Novoselov, Light-emitting diodes by band-structure engineering in van der Waals heterostructures, *Nat. Mater.* **14**, 301 (2015).
- [2] L.H. Fowler-Gerace, Zhiwen Zhou, E.A. Szwed, D.J. Choksy, L.V. Butov, Transport and localization of indirect excitons in a van der Waals heterostructure, *Nat. Photonics* **18**, 823 (2024).
- [3] Astrid Weston, Yichao Zou, Vladimir Enaldiev, Alex Summerfield, Nicholas Clark, Viktor Zólyomi, Abigail Graham, Celal Yelgel, Samuel Magorrian, Mingwei Zhou, Johanna Zultak, David Hopkinson, Alexei Barinov, Thomas H. Bointon, Andrey Kretinin, Neil R. Wilson, Peter H. Beton, Vladimir I. Fal'ko, Sarah J. Haigh, Roman Gorbachev, Atomic reconstruction in twisted bilayers of transition metal dichalcogenides, *Nat. Nanotechnol.* **15**, 592 (2020).
- [4] Matthew R. Rosenberger, Hsun-Jen Chuang, Madeleine Phillips, Vladimir P. Oleshko, Kathleen M. McCreary, Saujan V. Sivaram, C. Stephen Hellberg, Berend T. Jonker, Twist Angle-Dependent Atomic Reconstruction and Moiré Patterns in Transition Metal Dichalcogenide Heterostructures, *ACS Nano* **14**, 4550 (2020).
- [5] Shen Zhao, Zhijie Li, Xin Huang, Anna Rupp, Jonas Göser, Ilia A. Vovk, Stanislav Yu. Kruchinin, Kenji Watanabe, Takashi Taniguchi, Ismail Bilgin, Anvar S. Baimuratov, Alexander Högele, Excitons in mesoscopically reconstructed moiré heterostructures, *Nat. Nanotechnol.* **18**, 572 (2023).
- [6] Tomasz Woźniak, Paulo E. Faria Junior, Gotthard Seifert, Andrey Chaves, Jens Kunstmann, Exciton g factors of van der Waals heterostructures from first-principles calculations, *Phys. Rev. B* **101**, 235408 (2020).
- [7] William H. Press, Saul A. Teukolsky, William T. Vetterling, Brian P. Flannery, *Numerical recipes in C: the art of scientific computing (2nd ed.)*, Cambridge University Press (1992).
- [8] Daijiro Yoshioka, Allan H. MacDonald, Double quantum well electron-hole systems in strong magnetic fields, *J. Phys. Soc. Jpn.* **59**, 4211 (1990).
- [9] C.J. Dorow, M.W. Hasling, E.V. Calman, L.V. Butov, J. Wilkes, K.L. Campman, A.C. Gossard, Spatially resolved and time-resolved imaging of transport of indirect excitons in high magnetic fields, *Phys. Rev. B* **95**, 235308 (2017).
- [10] M. Remeika, J.C. Graves, A.T. Hammack, A.D. Meyertholen, M.M. Fogler, L.V. Butov, M. Hanson, A.C. Gossard, Localization-Delocalization Transition of Indirect Excitons in Lateral Electrostatic Lattices, *Phys. Rev. Lett.* **102**, 186803 (2009).
- [11] Zhiwen Zhou, E.A. Szwed, D.J. Choksy, L.H. Fowler-Gerace, L.V. Butov, Long-distance decay-less spin transport in indirect excitons in a van der Waals heterostructure, *Nat. Commun.* **15**, 9454 (2024).